Journal of Biomechanics 145 (2022) 111360

Contents lists available at ScienceDirect

Journal of Biomechanics

journal homepage: www.elsevier.com/locate/jbiomech

Increases in hydraulic conductance and solute permeability in a mouse model of ascending thoracic aortic aneurysm

Christie L. Crandall [a], Sean Y. Kim [b], Jacob Rother [a], Vivian S. Lee [c], Robert P. Mecham [c], Jessica E. Wagenseil [a,*]

[a] Department of Mechanical Engineering and Materials Science, Washington University, St. Louis, MO, United States
[b] Department of Biomedical Engineering, Saint Louis University, St. Louis, MO, United States
[c] Department of Cell Biology and Physiology, Washington University, St. Louis, MO, United States

ARTICLE INFO

Keywords:
Elastin
Diffusion
Solute
Mass transport
Lysyl oxidase
Thoracic aortic aneurysm

ABSTRACT

Large elastic arteries, such as the aorta, contain concentric layers of elastic laminae composed mainly of the extracellular matrix protein elastin. The structure of the elastic laminae could affect transmural mass transport and contribute to aortic disease progression. We studied the effects of a genetic mutation ($Lox^{M292R/+}$, referred to as MU) in mice associated with ascending thoracic aortic aneurysm (TAA) on the mass transport and elastic laminae structure. Solute absent fluid flux and hydraulic conductance through the ascending aortic wall were not significantly different between groups, however solute present fluid flux, hydraulic conductance, solute flux, and solute permeability of 4 kDa FITC-dextran were significantly increased in the MU group, indicating that movement of small molecules into the aortic wall is facilitated in MU mice. Quantification from light microscopy images of the ascending aorta showed no significant differences in wall thickness, or inner elastic lamina fenestration size and density, but an increase in the number of elastic laminae breaks in the MU group. Ultrastructural comparisons from transmission electron micrographs suggest less dense and disorganized elastic laminae in MU aorta that may also contribute to the transport differences. Our results provide an initial investigation into the connections between mass transport and elastic laminae structure, specifically in a genetic mouse aneurysm model, which can be further used to understand TAA pathology and develop treatment strategies.

1. Introduction

Thoracic aortic aneurysms (TAAs) are characterized by dilation of the aortic wall that may eventually lead to dissection and/or rupture. Genetic mutations can predispose individuals to TAAs, independent of, or coupled with other risk factors like hypertension and aging (Milewicz et al., 2017). In particular, genetic mutations that affect the formation, cross-linking, or structure of elastic fibers in the aortic wall are associated with the onset and progression of TAA. Elastic fibers are essential to maintain arterial integrity, as they allow elastic recoil necessary for normal cardiovascular function (Wagenseil and Mecham, 2009). Elastic fibers contain mostly cross-linked elastin and are organized in dense fibrous sheets called elastic laminae. The elastic laminae alternate with layers of smooth muscle cells (SMCs) throughout the middle (media) of the aortic wall. The inner layer (intima) contains endothelial cells (ECs) that interact with blood flow. The outer part (adventitia) contains mostly fibroblast cells and collagen fibers to provide strength and limit distension of the aortic wall.

Fenestrations, small pores, are present in the elastic laminae throughout the aortic wall but are largest and most distinct on the internal elastic lamina (IEL) that separates the intima and media. Genetic mutations that affect elastic fibers and are associated with TAA can affect the density and size of elastic laminae fenestrations (Lopez-Guimet et al., 2017). Although ECs are the most significant barrier to mass transport across the aortic wall, little attention has been given to transport through the media. In TAA, EC dysfunction is often present,

Abbreviations: TAA, thoracic aortic aneurysm; IEL, internal elastic lamina; LOX, lysyl oxidase; WT, wild-type; ATA, ascending thoracic aorta; PBS, phosphate buffered saline; SMC, smooth muscle cell; EC, endothelial cell; PG, proteoglycan; MMP, matrix metalloproteinase.

* Corresponding author at: Department of Mechanical Engineering and Materials Science, Washington University, One Brookings Dr., MSC 1185-208-125, St. Louis, MO 63130, United States.
E-mail address: jessica.wagenseil@wustl.edu (J.E. Wagenseil).

https://doi.org/10.1016/j.jbiomech.2022.111360
Accepted 21 October 2022
Available online 27 October 2022
0021-9290/© 2022 Elsevier Ltd. All rights reserved.

and so the media may play a more significant role in modulating transport (Sheremet'eva et al., 2004). Previously, we demonstrated that the elastic laminae structural integrity affects mass transport through the wall in mouse carotid arteries with altered elastic fiber structure (Cocciolone et al., 2018), but carotid arteries are generally not susceptible to aneurysms.

Mouse models with genetic mutations in elastic fiber proteins have been developed to better understand human TAA pathogenesis. Lysyl oxidase (LOX), an elastin and collagen cross-linking enzyme, is essential for the formation and homeostatic maintenance of the aortic wall and multiple mutations in LOX are associated with TAA (Guo et al., 2016). A heterozygous missense mutation in LOX associated with TAA was identified in humans and modeled in mice (c.857 T > G encoding p. M292R) (Lee et al., 2016). Homozygous $Lox^{M292R/M292R}$ mice die shortly after birth with TAA and severe cardiovascular abnormalities. Heterozygous $Lox^{M292R/+}$ mice have a longer, less compliant ascending aorta with an increased number of elastic laminae breaks. $Lox^{M292R/+}$ mice show increased aortic dilation in response to angiotensin-II (AngII) induced hypertension, suggesting that disrupted extracellular matrix combined with additional insults may contribute to TAA development (Lee et al., 2019). $Lox^{M292R/+}$ mice provide an experimental model to investigate how changes to the medial wall structure affect transmural mass transport, which may contribute to TAA pathogenesis or be leveraged for TAA therapies.

We investigated mass transport through the aortic wall in $Lox^{M292R/+}$ and wild-type (WT) mice. We hypothesized that structural defects in the elastic laminae of $Lox^{M292R/+}$ ascending aorta would decrease the resistance to solvent and solute transport across the aortic wall. We measured solvent and solute flux through the wall ex vivo under equivalent in vivo loading conditions and calculated hydraulic conductance and solute permeability. In addition, we imaged aortic samples in cross-section and en face with light and transmission electron microscopy to identify differences in elastic laminae organization, including laminae breaks, IEL fenestrae size and density, and laminae ultrastructure.

2. Methods

2.1. Mouse model and ultrasound imaging

Male and female $Lox^{M292R/+}$ mice (Lee et al., 2016) and WT littermates ages 4–5 months old were used (N = 13–17/group). The mice had osmotic pumps (Alzet model 1004, DURECT Corp.) with sterile saline implanted for 28 days before sacrifice. The saline treatment was originally a control for AngII treatment to induce hypertension that had technical challenges and so only the saline treated controls are presented here. The inner diameter of the ascending thoracic aorta (ATA) was measured using a Vevo 2100 ultrasound system (FUJIFILM Visualsonics) (N = 10–12/group). Mice were euthanized by carbon dioxide inhalation, the ATA was dissected, placed in phosphate buffered saline (PBS), and kept at 4 °C for up to four days (Amin et al., 2011) before transport measurements and light microscopy. An additional set of 3-month-old untreated, untested MU and WT ATAs (N = 3/group) were used for transmission electron microscopy. All animal protocols were approved by the Institutional Animal Care and Use Committee.

2.2. Transport theory

We define 1-D advection–diffusion mass transport through a semi-permeable membrane assuming 1-D transmural flow in response to a fluid pressure (ΔP) and solute gradient (Δc) (Kedem and Katchalsky, 1958). To describe the fluid flux (J_v), we combine the solvent transport described by hydraulic conductance (L_p) with the fluid pressure and the osmotic pressure due to the concentration gradient (Tedgui and Lever, 1984),

$$J_v = L_p(\Delta P - \sigma RT\Delta c) \quad (1)$$

where σ is a reflection coefficient, R is the gas constant, and T is the absolute temperature. Solute diffusivity is determined by the material's solute permeability (ω). Combining this with the average concentration of solute (c_s) moved by advection, we can calculate the solute flux (J_s),

$$J_s = \omega RT\Delta c + (1-\sigma')c_s J_v \quad (2)$$

where σ' is a reflection coefficient.

2.3. Transport measurements

A fluid column of PBS was connected to the inlet of a pressure myograph (Danish Myo Technology) 12+ hours before each experiment to allow system equilibration. An ATA (N = 13–17/group) was mounted in the pressure myograph using 7–0 sutures and placed in a bath of PBS at 37 °C (Fig. 1). ATAs were secured superior to the coronary arteries and anterior to the innominate artery. The ATA was stretched to an approximate in vivo axial stretch ratio of 1.1 (Wagenseil et al., 2005). ECs were disrupted by passing an air bubble through the ATA. Preliminary experiments confirmed that ECs were removed and SMCs were not active under our experimental conditions. The ATA was pressurized to 13.3 kPa (100 mmHg) by opening the fluid column inlet and the outer diameter was recorded. A bubble was introduced into the tubing and tracked to measure transmural fluid flow. After 30–60 min, the fluid column was emptied and replaced with 5 mg/mL 4 kDa FITC-Dextran in PBS (Sigma-Aldrich, #46944). The ATA was equilibrated for 30 min and then the outside of the ATA was rinsed and transferred to a new 7 mL bath of PBS. A bubble was introduced into the tubing and tracked for 70 min while two 50 μL samples were taken from the PBS bath every 10 min to measure concentration. Knowing the change in distance of the air bubble over time, the tubing inner diameter, and the measured ATA loaded dimensions, the fluid flux was calculated (Baldwin et al., 1992) for each ATA when the solute was absent (J_v) and present (J_{vs}). By plotting the change in concentration over time of the external bath, the slope was used to calculate solute flux (J_s) (Cocciolone et al., 2018). A diagram of the experimental set-up is shown in Fig. 1.

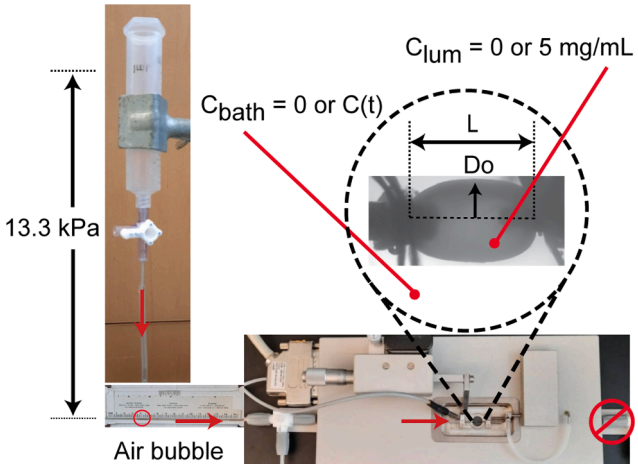

Fig. 1. Experimental set-up. The ATA was mounted in a pressure myograph and secured with 7–0 sutures. It was stretched to 1.1 axial stretch ratio and pressurized to 13.3 kPa (100 mmHg) by a static fluid pressure column of PBS. Length (L) and outer diameter (D_o) were recorded. An air bubble was inserted into the tubing to track fluid flux through the wall. Both solute absent (C_{lum} = C_{bath} = 0) and solute present (C_{lum} = 5 mg/mL 4 kDa FITC-dextran and C_{bath} = measured C(t)) experiments were performed for each ATA.

2.4. Transport analysis

We assume that the reflection coefficients (σ, σ') are equal, based on the Onsager reciprocal relationship, and that the value must be between 1 (ATA is impermeable to solute) and 0 (ATA is equally permeable to solvent and solute) (Cussler, 2009). Resolution of the individual ATA experiments was not sufficient to calculate σ from the J_{vs} data assuming L_p from the J_v data (Eqn. (1)). Comparison of the J_s and J_{vs} data for each ATA to the other terms in Eqn. (2) demonstrated that $\omega < 0$ for at least one ATA for all values of $\sigma' < 0.99$. Because there was measurable J_s, we know that $\sigma' \neq 1$, so we chose the lowest value that could be applied to all ATAs and set $\sigma = \sigma' = 0.99$. These values are similar to those assumed for transport of 67 kDa albumin across the wall of the rabbit common carotid artery (Karmakar and Lever, 1994). We calculated solute absent (L_p) and present (L_{p_s}) hydraulic conductance and solute permeability (ω) for each ATA.

2.5. Wall structure imaging and quantification

For light microscopy, post-experimentation ATAs were fixed in 4 % paraformaldehyde for 10–24 h while maintained at 13.3 kPa with a PBS fluid column. After fixation, the ATAs were sequentially dehydrated, then rehydrated, and either flash-frozen in O.C.T. compound and cut into 15 μm cross-sections (N = 4/group) or sliced transversely along the anterior midline, in line with both the basal end and innominate artery for en face (intimal surface) imaging (N = 3/group). The ATA samples were placed onto slides and cover slipped.

Cross-sections were imaged with an Olympus FV1000MPE multiphoton microscope with a 25× objective. Collagen and elastin were excited at 880 nm and imaged using second-harmonic generation (emission: 420–460 nm) and autofluorescence (emission: 495–540 nm), respectively. Laminae breaks were quantified by three blinded individuals (Lee et al., 2016) using ImageJ (NIH). Determination of breaks compared to out of plane (and hence less bright) regions was subjective. In most cases, 2/3 of the individual measurements for an image were similar, hence the closest two blinded measurements were averaged for each image, providing an average variance of 1.4 %. Wall thickness was measured using the line-draw tool and values reported are averaged for three locations.

En face sections were imaged with a Leica Sp-8 DIVE multiphoton microscope with a 40× objective to visualize the IEL (excitation: 880 nm, emission: 495–540 nm) with two images taken left and right of the posterior midline (inner curvature) for each ATA. Z-stacks were taken with 0.2 μm distance and then projected for the entire IEL thickness. Three 17.2 × 17.2 μm^2 areas per image were chosen manually by a blinded individual, allowing analysis of only portions where the wavy IEL was entirely in-plane. Fenestrations were isolated in ImageJ manually using the Thresholding and Despeckle functions to create a binary mask which was used calculate area and density of the fenestrations in Matlab (Mathworks). Values from the four images (total 12 areas/ATA) were averaged per ATA.

For transmission electron microscopy (N = 3/group), 3 month old untreated WT and MU mice were sacrificed and perfused with PBS through the left ventricle. The untested ATA was excised and fixed in 2.5 % glutaraldehyde and 0.1 M sodium cacodylate solution overnight at 4 °C. The samples were further processed, sectioned, and imaged on a Jeol 1400 Electron Microscope at the Washington University Center for Cellular Imaging (Lee et al., 2016).

2.6. Statistical analysis

Data analysis was conducted using GraphPad Prism. Two and one outlier(s) were removed from the solute absent and solute present data, respectively, using the ROUT test. Using a 2-way ANOVA with Sidak's posthoc test we found a significant effect of sex on MU outer diameter, but no significant effect on the transport parameters. There were not enough males and females in each group to determine the significant effect of sex on the in vivo inner diameters or wall structure. As we were focused on transport differences, we combined male and female data for each experimental group. Data were compared using an unpaired or paired *t*-test, as appropriate. P-values < 0.05 were considered significant.

3. Results

ATA lumen inner diameters were measured in vivo by ultrasound before sacrifice. The systolic inner diameters are 9.8 % smaller in MU mice (Fig. 2A), while there are no significant differences in diastolic inner diameters (Fig. 2B). Smaller systolic diameters with equal diastolic diameters implies a stiffer or less compliant aorta, with less diameter change due to pressure increases during the cardiac cycle (Le and Wagenseil, 2012). ATA lengths and outer diameters were measured when loaded at a 1.1x axial stretch ratio and 13.3 kPa (100 mmHg) internal pressure. MU ATA length is increased 17 % (Fig. 2C), while outer diameter is similar to WT (Fig. 2D). Note that the in vivo systolic and diastolic inner diameter measurements show trends for the MU ATA to be smaller than WT, while the ex vivo outer diameter measurements show no difference in MU ATA compared to WT. These measurements suggest that the wall thickness is increased in MU ATA. There is a 16 % increase in outer diameters of MU male mice compared to female mice (Supp. Fig. 1).

For the transport experiments, plots of air bubble movement vs time (Fig. 3A and B) were used to calculate fluid flux in the absence (Fig. 3D) and presence (Fig. 3E) of solute. The fluid flux is not significantly different between groups for the solute absent experiments (Fig. 3D) but is 54 % higher in the MU group for the solute present experiments

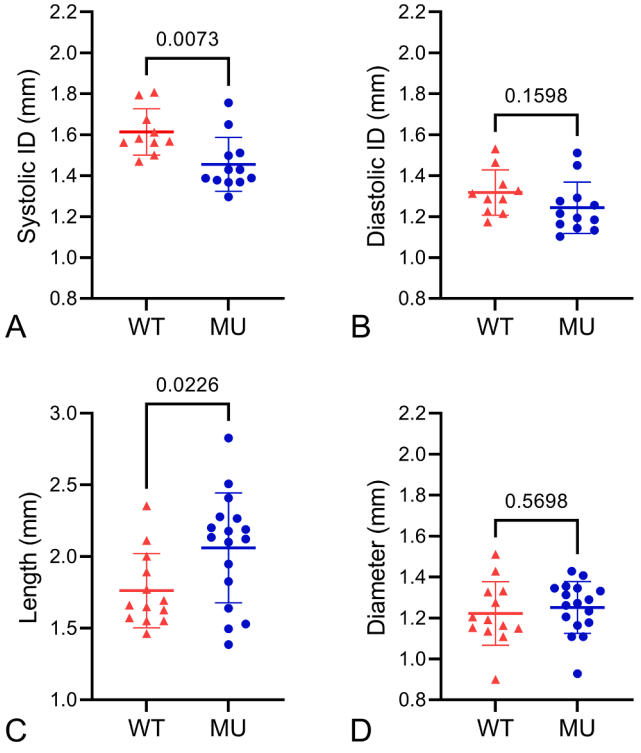

Fig. 2. ATA dimensions. Ultrasound measurements of in vivo ATA inner diameter (ID) at systole (A) and diastole (B). N = 10 wt, 12 MU. ATA lengths at 1.1x axial stretch ratio (C) and outer diameters at 13.3 kPa (100 mmHg) (D) when mounted ex vivo in a pressure myograph for the transport experiments. N = 13 wt, 17 MU. P-values from t-tests, individual data points, and mean ± SD are shown.

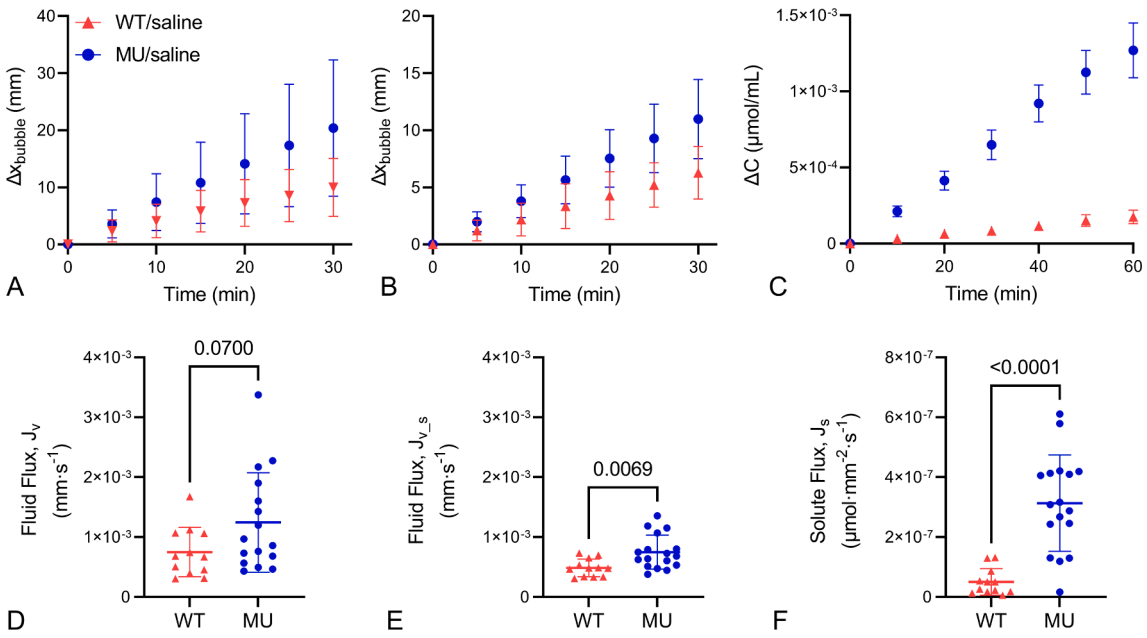

Fig. 3. Transport data. Average bubble movement vs time for solute absent (A) and present (B) transport experiments. Concentration vs time of the external PBS bath for solute present transport experiments (C). Data were normalized to begin with zero bubble movement and zero concentration in the bath. Data in A–C were used to calculate fluid flux with solute absent (D), fluid flux with solute present (E), and solute flux (F). For A–C mean ± SD are shown. For D–F, P-values from t-tests, individual data points, and mean ± SD are shown. N = 12 wt, 16–17 MU.

(Fig. 3E). The concentration of the external bath vs time (Fig. 3C) was used to calculate the solute flux (Fig. 3F), which is increased 521 % in the MU groups. Data were normalized to assume zero bubble movement and zero concentration at time = 0 min. Steady-state fluid and solute fluxes are evident by the linearity of these measurements over time (Fig. 3A–C).

The measurements of fluid flux, solute flux, and change in concentration over time were used in Equations (1) and (2) to calculate solute permeability and hydraulic conductance for each ATA. No significant differences are present in the solute absent hydraulic conductance values, although they trend higher in the MU ATA (Fig. 4A). MU solute present hydraulic conductance increases by 54 % compared to WT (Fig. 4B). Paired comparisons of the solute absent and solute present hydraulic conductance values for each ATA show no significant differences (Supp. Fig. 2). MU solute permeability is 552 % higher than WT (Fig. 4C).

Using multiphoton imaging, we quantified elastic laminae structure from cross-sectional and en face images. Fig. 5 shows representative cross-sectional images from WT and MU samples and quantification of laminae breaks in each group. MU ATA has 61 % more laminae breaks than WT (Fig. 5C), but no significant differences in layer thicknesses (Supp. Fig. 3). Fig. 6 shows an en face ATA image and fenestrae quantification. Neither fenestrae area nor density are significantly different. We found no significant differences between fenestrae measurements based on localization (left or right of posterior midline).

Using transmission electron microscopy, we investigated ultrastructural differences in the elastic laminae. In the WT ATA, dense, smooth elastic laminae are seen between layers of SMCs with an occasional break in the laminae (Fig. 7A). In the MU ATA, the laminae are less dense and have rough edges, with small breaks or areas of disorganized elastin deposition (Fig. 7B).

4. Discussion

Previously, we found increased mass transport with elastic fiber fragmentation in mouse carotid arteries (Cocciolone et al., 2018; Guang et al., 2022), which was limiting in terms of better understanding TAA progression and treatment since carotid arteries do not typically develop aneurysms. Here, we studied mass transport in the mouse ATA with a genetic mutation associated with TAA and elastic fiber fragmentation (Lee et al., 2019; Lee et al., 2016). With a concentration gradient present, the MU ATA has higher fluid flux, solute flux, hydraulic

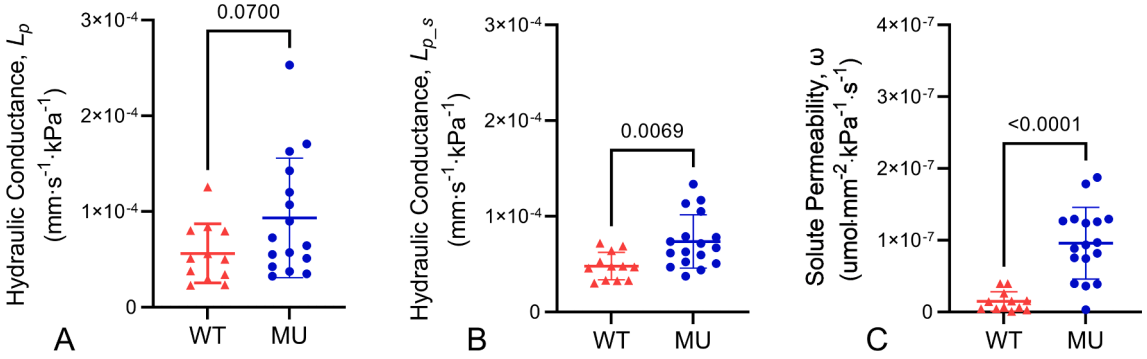

Fig. 4. Transport parameters. Calculated values for hydraulic conductance from solute absent (A) and solute present (B) transport experiments and solute permeability (C). P-values from t-tests, individual data points, and mean ± SD are shown. N = 12 wt, 16–17 MU.

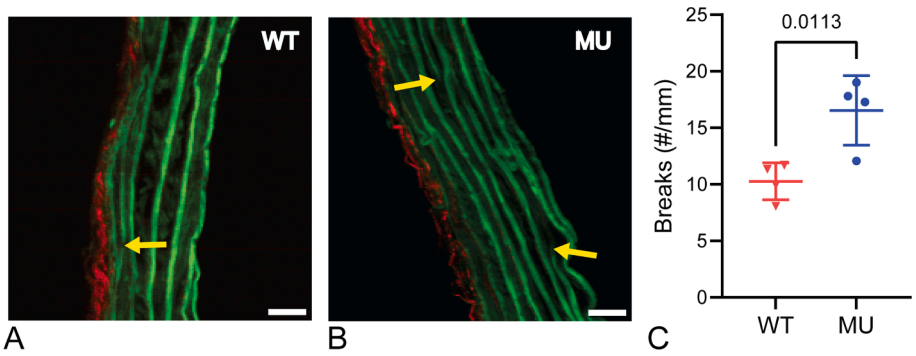

Fig. 5. Representative cropped multiphoton images of cross-sections for WT (A) and MU (B) ATA. Elastin is shown in green, collagen in red. Scale bar = 20 μm. Yellow arrows point to breaks in laminae that were quantified for each genotype from multiple cross-sectional images per ATA (C) (N = 4 ATAs/group). P-values from t-tests, individual data points, and mean ± SD are shown. (For interpretation of the references to colour in this figure legend, the reader is referred to the web version of this article.)

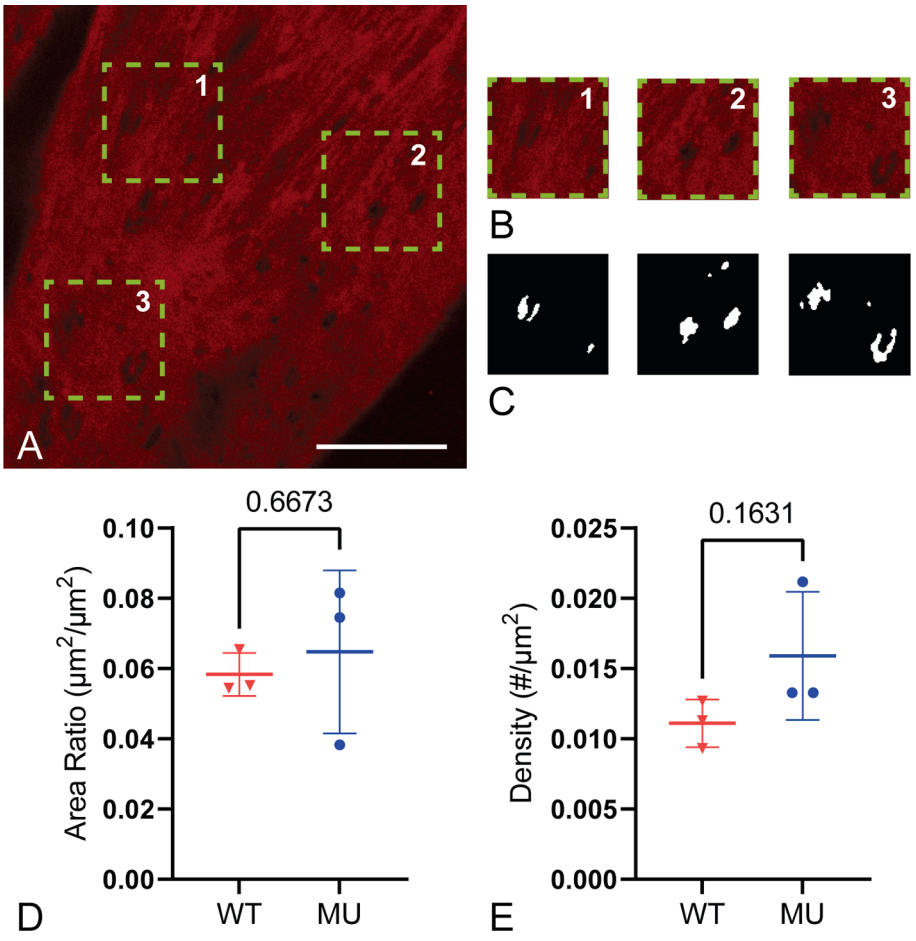

Fig. 6. Representative multiphoton image of an en face ATA with the three areas chosen for IEL fenestrae quantification (A), the three analyzed areas (B), and their corresponding mask of fenestrae holes (C). Red fluorescence is elastin, large dark areas are where the IEL goes out of the image plane, and small dark areas are fenestrae. Scale bar = 20 μm. Four images (A) and three cropped image areas (B) were quantified for each ATA and averaged. The area ratio of fenestrae to IEL and density of fenestrae holes were quantified (D–E) (N = 3 ATAs/group). P-values from t-tests, individual data points, and mean ± SD are shown. (For interpretation of the references to colour in this figure legend, the reader is referred to the web version of this article.)

conductance, and solute permeability compared to WT, indicating facilitated movement of solvents and solutes across the ATA wall.

Previous studies showed increased length, wall thickness, and number of elastic laminae breaks in the MU ATA compared to WT (Lee et al., 2019; Lee et al., 2016). We also found increased ATA length (Fig. 2C) and number of elastic laminae breaks (Fig. 5C). We did not show an increase in MU wall thickness (Supp. Fig. 3), but our inner and outer diameter measurements (Fig. 2) suggest that there could be thickness increases in the MU ATA. Although, this does not account for connective tissue which may have been removed during excision. Previously reported increases in MU ATA wall thickness were not quantified. Lee et al. (2016) showed a stiffer MU ATA, as suggested by our systolic and diastolic inner diameter measurements (Fig. 2A and B). Lee et al. (2019) showed increased diameter dilation of the MU ATA compared to WT in response to AngII-induced hypertension, indicating that additional insults in conjunction with elastic fiber fragmentation may contribute to TAA formation. We attempted to induce aneurysms with AngII-induced hypertension in our MU mice, but due to technical difficulties were not able to confirm effectiveness of the AngII treatment and so chose to focus only on the saline treated controls and effects of the genetic mutation alone.

We chose the MU mouse because it models a heterozygous human mutation that causes disorganized elastic fibers and TAA, has structural differences in extracellular matrix organization, does not form TAA under normal conditions and hence will not have major geometric changes that may complicate our comparisons to WT (Lee et al., 2016), and can form TAA with additional insults such as AngII-induced hypertension (Lee et al., 2019). Our goal was to investigate mass transport differences that could contribute to TAA progression or be leveraged for treatment. There are differences between mice and humans that must be

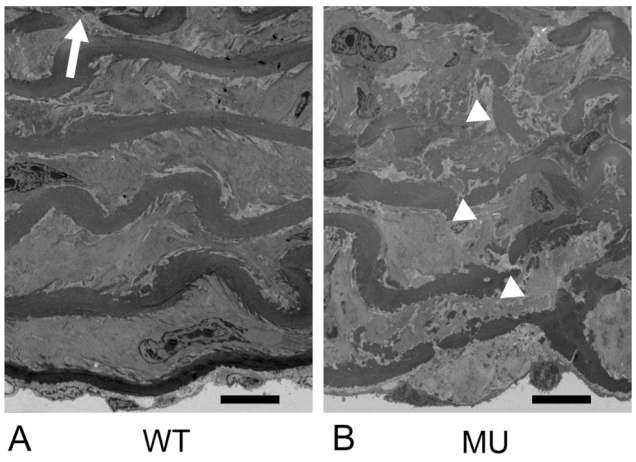

Fig. 7. Representative transmission electron micrograph of WT (A) and MU (B) ATA cross-sections. The intima is at the bottom of the images. Elastic laminae alternate with layers of SMCs. Sparse, clear laminae breaks can be seen in WT ATA (arrow), while the rest of the laminae are smooth and continuous. Breaks in MU ATA (arrowheads) are more numerous, but less distinct due to overall disorganization of the laminae structure. N = 3/genotype examined. Scale bar = 10 μm.

considered, in particular, only mice with the homozygous mutation get TAA without additional insults, but they die at birth. Additionally, humans have thicker ATA walls (2 mm vs 100 μm), many more elastic laminae (60 vs 10) (Wolinsky, 1970), and a vasa vasorum (capillary network in the adventitia), all of which may lead to differences in mass transport properties of human compared to mouse ATA. Nevertheless, human TAA pathogenesis has been linked to circulating molecules (such as TGFβ) (Milewicz et al., 2017) and cells (such as monocytes) (Kim et al., 2020) that may distribute differentially within the diseased media due to increased mass transport linked to elastic fiber defects.

Fenestrations in the arterial wall are hypothesized to aid in mass transport. We did not see significant differences between genotypes when measuring IEL fenestrae areas or density using light microscopy. Our measured area of the IEL fenestrations (average of 1.85 μm^2) is comparable to other studies (Lopez-Guimet et al., 2017; Tada and Tarbell, 2004). Differences in fenestrae size and density have been reported in hypertensive rat aorta (Boumaza et al., 2001) and in other genetic TAA mouse models that affect elastic fiber structure (Lopez-Guimet et al., 2017). Additional work is needed to determine if fenestrae area or density in the WT and MU ATA changes with applied pressures beyond 13.3 kPa or in elastic laminae beyond the IEL. We did see an increase in medial elastic laminae breaks (Fig. 5C) in MU ATA that may facilitate mass transport. Additionally, electron microscopy shows elastic laminae disorganization at the ultrastructural level in MU ATA (Fig. 7) that may further assist in the movement of solvents and solutes across the aortic wall.

The calculated values for hydraulic conductance in WT ATA (Fig. 4A and B) agree with our previous study in mouse carotid arteries (Cocciolone et al., 2018) and are an order of magnitude higher than studies in rabbit and rat descending aorta with no ECs (Shou et al., 2006; Tedgui and Lever, 1984). We do not believe that increased hydraulic conductance in our studies is due to leaks in the experimental set-up, as preliminary experiments with 2000 kDa blue dextran (which does not diffuse through the wall) showed no change in concentration in the outer bath over time. Preliminary experiments also showed that SMCs were inactive during our experiments, which may have contributed to the higher hydraulic conductance. The differences may otherwise be due to animal specific alterations in wall structure and extracellular matrix organization that require further investigation. Our calculated solute permeability values in WT ATA (Fig. 4C) are similar to those from our previous work on mouse carotid arteries (Cocciolone et al., 2018) if the reflection coefficients = 0.99. Our solute permeability values are two orders of magnitude higher than those calculated for cells (He and Devireddy, 2005), suggesting that the solute is moving around and not through the cells.

The solute permeability values depend on our chosen reflection coefficients, which could not be calculated due to limitations in the resolution and repeatability of the transport measurements in the small mouse ATA. The challenges in performing these experiments are evident in the data variability, which is greater than previous work on larger animal models (Shou et al., 2006; Tedgui and Lever, 1984). Data variability is increased in MU compared to WT ATA, which is consistent with features of genetically modified mice with identical genetics, but variable phenotypes. Because transport parameters were normalized to ATA geometry, sex differences specific to the MU ATA could have contributed to the data variability. Data variability is decreased in the solute present experiments (i.e. Fig. 4A and B), which may be due to additional ATA equilibration time after adding solute. Preliminary studies which measured leakage using blue dextran and confirmed SMC inactivity were not performed on each ATA. Differences in these factors per ATA may have contributed to the variability. Despite these limitations, our study provides mass transport parameters for the mouse ATA wall that are significantly affected by a genetic mutation that is associated with TAA in humans.

The transport parameters for WT and MU ATA can be used in computational models to investigate additional conditions such as axial mass transport (Hwang and Edelman, 2002) or the effects of solute size or aortic geometry. Hypertensive blood pressures could also be modeled (Xue et al., 2005). Previous computational modeling assumed the IEL to be an impermeable membrane with permeable fenestrations (Yuan et al., 1991). We argue that the IEL fenestrations are not the only porous mechanism in the aortic wall and it may be advantageous to couple current models of permeable fenestrations (Tada and Tarbell, 2004) with a semipermeable media (Guang et al., 2022) to better understand the relationship between TAA genetic mutations and mass transport differences. Especially as the TAA mutation we investigated, and others, affect elastic fiber crosslinking or ultrastructure throughout the wall, and not just IEL fenestrae area and/or density.

Solvent and solute transport are significantly higher in MU compared to WT ATA when a concentration gradient is present. Beyond structural and ultrastructural differences in the elastic laminae, the mass transport differences may be linked to the proteoglycan (PG) content of the wall. PGs have high water uptake abilities, which can create pathways for transport (Van den Berg, 2012). PGs do not take up the stains used in our electron micrographs (Fig. 7), hence the lighter colored areas within the disorganized MU elastic laminae may contain PGs. A greater PG content is associated with TAA pathogenesis and can cause stress concentrations that drive TAA dissection (Roccabianca et al., 2014; Shen et al., 2019). In addition, both a reduction in SMCs and an increase in matrix metalloproteinases (MMPs) are associated with TAA pathology (Borges et al., 2009; Ikonomidis et al., 2005). SMCs and MMPs can travel by diffusion or PG pathways, which may be substantial in a more permeable membrane (Stamenkovic, 2003). The diameter of the 4 kDa solute (2.8 nm) is six orders of magnitude smaller than our fenestrae areas and more similar to PG's size of 10–270 kDa. Therefore, PG pathways may affect small molecule transport more than fenestrations. Further work would need to quantify PGs, cells, MMPs, and stresses within the extracellular matrix of the MU ATA to relate these mechanisms to TAA pathology.

Overall, we show increases in mass transport across the aortic wall in a TAA mouse genetic model compared to WT control. Limitations of our study include differences between human and mouse aorta, not introducing additional risk factors (i.e. AngII-induced hypertension) to push the MU ATA dilation, assumptions required for the reflection coefficients to calculate solute permeability, and high variability in the transport measurements due to the small size of the mouse ATA. Future studies are needed to investigate the impact of PGs and the wall composition and ultrastructure, beyond IEL fenestrations, as a barrier to

mass transport. The studies could also be expanded to other mouse models of TAA (Bellini et al., 2017; Cebull et al., 2020) to determine if the results are repeatable and consistent among different genetic mutations linked to TAA. Our current results and future studies can help us to better understand mass transport in TAA associated with genetic mutations affecting the extracellular matrix and to guide drug design and targeting for TAA treatment.

CRediT authorship contribution statement

Christie L. Crandall: Writing – review & editing, Writing – original draft, Supervision, Methodology, Investigation, Formal analysis, Data curation. **Sean Y. Kim:** Methodology, Investigation, Formal analysis. **Jacob Rother:** Methodology, Investigation, Formal analysis. **Vivian S. Lee:** Methodology, Investigation, Data curation. **Robert P. Mecham:** Writing – review & editing, Funding acquisition. **Jessica E. Wagenseil:** Writing – review & editing, Writing – original draft, Supervision, Project administration, Funding acquisition, Formal analysis, Data curation, Conceptualization.

Declaration of Competing Interest

The authors declare that they have no known competing financial interests or personal relationships that could have appeared to influence the work reported in this paper.

Data availability

All data is included in the published manuscript or references.

Acknowledgements

This study was partially funded be the American Heart Association (19TPA-34910047, JEW) and the National Institutes of Health (HL53325, RPM).

Appendix A. Supplementary material

Supplementary data to this article can be found online atzhttps://doi.org/10.1016/j.jbiomech.2022.111360.

References

Amin, M., Kunkel, A.G., Le, V.P., Wagenseil, J.E., 2011. Effect of storage duration on the mechanical behavior of mouse carotid artery. J. Biomech. Eng. 133, 071007.
Baldwin, A.L., Wilson, L.M., Simon, B.R., 1992. Effect of pressure on aortic hydraulic conductance. Arterioscler. Thromb. 12, 163–171.
Bellini, C., Bersi, M.R., Caulk, A.W., Ferruzzi, J., Milewicz, D.M., Ramirez, F., Rifkin, D. B., Tellides, G., Yanagisawa, H., Humphrey, J.D., 2017. Comparison of 10 murine models reveals a distinct biomechanical phenotype in thoracic aortic aneurysms. J. R. Soc. Interface 14.
Borges, L.F., Touat, Z., Leclercq, A., Zen, A.A., Jondeau, G., Franc, B., Philippe, M., Meilhac, O., Gutierrez, P.S., Michel, J.B., 2009. Tissue diffusion and retention of metalloproteinases in ascending aortic aneurysms and dissections. Hum. Pathol. 40, 306–313.
Boumaza, S., Arribas, S.M., Osborne-Pellegrin, M., McGrath, J.C., Laurent, S., Lacolley, P., Challande, P., 2001. Fenestrations of the carotid internal elastic lamina and structural adaptation in stroke-prone spontaneously hypertensive rats. Hypertension 37, 1101–1107.
Cebull, H.L., Rayz, V.L., Goergen, C.J., 2020. Recent advances in biomechanical characterization of thoracic aortic aneurysms. Front. Cardiovasc. Med. 7, 75.
Cocciolone, A.J., Johnson, E., Shao, J.Y., Wagenseil, J.E., 2018. Elastic fiber fragmentation increases transmural hydraulic conductance and solute transport in mouse arteries. J. Biomech. Eng.
Cussler, E.L., 2009. Diffusion: Mass Transfer in Fluid Systems, third ed. Cambridge University Press.
Guang, Y., Cocciolone, A.J., Crandall, C.L., Johnston, B.B., Setton, L.A., Wagenseil, J.E., 2022. A multiphasic model for determination of water and solute transport across the arterial wall: effects of elastic fiber defects. Arch. Appl. Mech. 92, 447–459.
Guo, D., Regalado, E.S., Gong, L., Duan, X., Santos-Cortez, R.L., Arnaud, P., Ren, Z., Cai, B., Hostetler, E.M., Moran, R., Liang, D., Estrera, A.L., Safi, H.J., Leal, S.M., Bamshad, M.J., Shendure, J., Nickerson, D.A., Jondeau, G., Boileau, C., Milewicz, D. M., 2016. LOX mutations predispose to thoracic aortic aneurysms and dissections. Circ. Res.
He, Y., Devireddy, R.V., 2005. An inverse approach to determine solute and solvent permeability parameters in artificial tissues. Ann. Biomed. Eng. 33, 709–718.
Hwang, C.W., Edelman, E.R., 2002. Arterial ultrastructure influences transport of locally delivered drugs. Circ. Res. 90, 826–832.
Ikonomidis, J.S., Barbour, J.R., Amani, Z., Stroud, R.E., Herron, A.R., McClister Jr., D.M., Camens, S.E., Lindsey, M.L., Mukherjee, R., Spinale, F.G., 2005. Effects of deletion of the matrix metalloproteinase 9 gene on development of murine thoracic aortic aneurysms. Circulation 112, I242–I248.
Karmakar, N., Lever, M.J., 1994. Effects of high molecular weight solutes on fluid flux across the arterial wall. Heart Vessels 9, 275–282.
Kedem, O., Katchalsky, A., 1958. Thermodynamic analysis of the permeability of biological membranes to non-electrolytes. BBA 27, 229–246.
Kim, A.J., Xu, N., Umeyama, K., Hulin, A., Ponny, S.R., Vagnozzi, R.J., Green, E.A., Hanson, P., McManus, B.M., Nagashima, H., Yutzey, K.E., 2020. Deficiency of circulating monocytes ameliorates the progression of myxomatous valve degeneration in Marfan syndrome. Circulation 141, 132–146.
Le, V.P., Wagenseil, J.E., 2012. Echocardiographic characterization of postnatal development in mice with reduced arterial elasticity. Cardiovasc. Eng. Technol. 3, 424–438.
Lee, V.S., Halabi, C.M., Broekelmann, T.J., Trackman, P.C., Stitziel, N.O., Mecham, R.P., 2019. Intracellular retention of mutant lysyl oxidase leads to aortic dilation in response to increased hemodynamic stress. JCI Insight 5.
Lee, V.S., Halabi, C.M., Hoffman, E.P., Carmichael, N., Leshchiner, I., Lian, C.G., Bierhals, A.J., Vuzman, D., Brigham Genomic, M., Mecham, R.P., Frank, N.Y., Stitziel, N.O., 2016. Loss of function mutation in LOX causes thoracic aortic aneurysm and dissection in humans. Proc. Natl. Acad. Sci. U. S. A.
Lopez-Guimet, J., Andilla, J., Loza-Alvarez, P., Egea, G., 2017. High-resolution morphological approach to analyse elastic laminae injuries of the ascending aorta in a murine model of Marfan syndrome. Sci. Rep. 7, 1505.
Milewicz, D.M., Prakash, S.K., Ramirez, F., 2017. Therapeutics targeting drivers of thoracic aortic aneurysms and acute aortic dissections: insights from predisposing genes and mouse models. Annu. Rev. Med. 68, 51–67.
Roccabianca, S., Ateshian, G.A., Humphrey, J.D., 2014. Biomechanical roles of medial pooling of glycosaminoglycans in thoracic aortic dissection. Biomech. Model. Mechanobiol. 13, 13–25.
Shen, Y.H., Lu, H.S., LeMaire, S.A., Daugherty, A., 2019. Unfolding the story of proteoglycan accumulation in thoracic aortic aneurysm and dissection. Arterioscler. Thromb. Vasc. Biol. 39, 1899–1901.
Sheremet'eva, G.F., Ivanova, A.G., Belov Iu, V., Gens, A.P., Kocharian, E.Z., 2004. A comparative study of the aortic wall in patients with Marfan's syndrome and Erdheim's disease. Angiol. Sosud. Khir. 10, 22–29.
Shou, Y., Jan, K.M., Rumschitzki, D.S., 2006. Transport in rat vessel walls. I. Hydraulic conductivities of the aorta, pulmonary artery, and inferior vena cava with intact and denuded endothelia. Am. J. Physiol. Heart Circ. Physiol. 291, H2758–H2771.
Stamenkovic, I., 2003. Extracellular matrix remodelling: the role of matrix metalloproteinases. J. Pathol. 200, 448–464.
Tada, S., Tarbell, J.M., 2004. Internal elastic lamina affects the distribution of macromolecules in the arterial wall: a computational study. Am. J. Physiol. Heart Circ. Physiol. 287, H905–H913.
Tedgui, A., Lever, M.J., 1984. Filtration through damaged and undamaged rabbit thoracic aorta. Am. J. Physiol. 247, H784–H791.
Van den Berg, F., 2012. 4.3 - Extracellular matrix. In: Schleip, R., Findley, T.W., Chaitow, L., Huijing, P.A. (Eds.), Fascia: The Tensional Network of the Human Body. Churchill Livingstone, Oxford, pp. 165–170.
Wagenseil, J.E., Mecham, R.P., 2009. Vascular extracellular matrix and arterial mechanics. Physiol. Rev. 89, 957–989.
Wagenseil, J.E., Nerurkar, N.L., Knutsen, R.H., Okamoto, R.J., Li, D.Y., Mecham, R.P., 2005. Effects of elastin haploinsufficiency on the mechanical behavior of mouse arteries. Am. J. Physiol. Heart Circ. Physiol. 289, H1209–H1217.
Wolinsky, H., 1970. Comparison of medial growth of human thoracic and abdominal aortas. Circ. Res. 27, 531–538.
Xue, B., Pamidimukkala, J., Hay, M., 2005. Sex differences in the development of angiotensin II-induced hypertension in conscious mice. Am. J. Physiol. Heart Circ. Physiol. 288, H2177–H2184.
Yuan, F., Chien, S., Weinbaum, S., 1991. A new view of convective-diffusive transport processes in the arterial intima. J. Biomech. Eng. 113, 314–329.